Transport barrier in 5D gyrokinetic flux-driven simulations

G. Lo-Cascio[1], E. Gravier[1], M. Lesur[1], Y. Sarazin[2], X. Garbet[2], L. Vermare[3], K. Lim[4], A. Guillevic[1], T. Réveillé[1], and V. Grandgirard[2]

[1]Université de Lorraine, CNRS, IJL, F-54000 Nancy, France
[2]CEA, IRFM, F-13108 Saint-Paul-lez-Durance, France
[3]Ecole Polytechnique, LPP, CNRS UMR 7648, 91128 Palaiseau, France
[4]Swiss Plasma Center, CH-1015 Lausanne, Switzerland

April 20, 2022

Abstract

Two ways for producing a transport barrier through strong shear of the $\mathbf{E}\times\mathbf{B}$ poloidal flow have been investigated using GYSELA gyrokinetic simulations in a flux-driven regime. The first one uses an external poloidal momentum (i.e vorticity) source that polarizes locally the plasma, and the second one enforces a locally steep density profile that also stabilizes the Ion Temperature Gradient (ITG) instability modes linearly. Both cases show a very low local turbulent heat diffusivity coefficient χ_T^{turb} and an increase in core pressure when a threshold of $\omega_{E\times B} \approx 3\overline{\gamma}_{lin}$ (respectively the $E\times B$ shear rate and average linear growth rate of ITG) is reached, validating previous numerical results. This pressure increase and χ_T quench are the signs of a transport barrier formation. This behaviour is a result of a reduced turbulence intensity which strongly correlates with the shearing of turbulent structures as evidenced by a reduction of the auto-correlation length of potential fluctuations as well as an intensity reduction of the k_θ spectra. Moreover, a small shift towards smaller poloidal wavenumber is observed in the vorticity source region which could be linked to a tilt of the turbulent structures in the poloidal direction.

1 Introduction

Transport is an important topic in magnetic confinement fusion devices because of its impact on the reactor efficiency. On top of the neoclassical transport [1] (i.e outward radial transport), the dominant loss channel is the anomalous [2][3][4] (i.e turbulent) one. This anomalous transport is mainly due to micro-instabilities [5] [6] leading to large values of heat conductivity and radial heat fluxes. Ion Temperature Gradient (ITG) [7][8] and Trapped Electron Modes (TEM) [9][10] in the core region or Kelvin-Helmoltz and Rayleigh-Taylor modes in the separatrix region are exemples of such instabilities.

However, overall transport can be reduced (i.e increasing confinement time) by triggering a plasma transition to a higher confinement state. Such transition, usually called

"Low-to-High transition" [11][12][13] (L-H transition), is a bifurcation of the plasma state observed experimentally in many tokamaks, e.g DIII-D [14][15], JFT-2M [16], Alcator C-mod [17], JET [18], ASDEX [11] and ASDEX Upgrade [19][20], COMPASS [21] or MAST [22], characterized by edge transport barriers (ETB) in H-mode. Their triggering occurs when a certain power threshold is exceeded and exhibit many interesting properties such as a very steep pressure gradient and a strong radial electric field. As a result a strong poloidal $E \times B$ sheared flow is generated. Part of this shearing (i.e zonal flows [23] [24] [25]) is generated by turbulence and leads to a self-regulated state through a prey-predator mechanism [26]. The main interest of this article is to invstigate the effect of a locally imposed flow shear on ITG modes and its radial structures.

The effects of flow shear on a turbulent plasma have been studied [27] [28] [29] using different theoretical explanations for the underlying mechanisms leading to a turbulence quench. The main hypothesis which will be explored here is that large scale turbulent structures are suppressed and teared by an $R\times B$ poloidal shearing. The decorrelation rate of the turbulence, both spatial and temporal, is then largely increased by sheared flows and reduces the transport locally as a result of lower turbulence intensity. An empiric criteria gives an estimate of $\omega_{E\times B}$, the $E \times B$ shear rate, which should within the same order as γ_{lin}^{max}, the maximum linear growth rate of the instability.

We propose here to extend a previous study of A. Strugarek [30] [31] using an updated version of GYSELA, a full-f 5D gyrokinetic code, using the same vorticity source to produce a sheared poloidal momentum profile. In section 2, we give a brief description of the model used in GYSELA and the construction of the vorticity source term used. Simulation conditions and parameters are given in section 3. Section 4 is dedicated to the onset of a transport barrier using the vorticity source. Section 5 focuses on a transport barrier triggered by a fixed steep density gradient profile. A conclusion is provided in section 6.

2 Model and source term

GYSELA [32] is a 5D full-f gyrokinetic [33] electrostatic code coupling the Vlasov equation and the quasi-electroneutrality equation. The electron density response is taken adiabatic so that, up to compressible effects, time-averaged particle transport across circular magnetic surfaces vanishes. The following set of equations are solved for Deuterium particles:

$$B_{\parallel}^{\star}\partial_t \bar{F} + \nabla \cdot \left(\dot{\mathbf{x}}_{GC} B_{\parallel}^{\star} \bar{F}\right) + \partial_{v_{G\parallel}} \left(\dot{v}_{G\parallel} B_{\parallel}^{\star} \bar{F}\right) = \mathcal{C}\left(\bar{F}\right) + \mathcal{S}, \tag{1}$$

$$en_{e_0}\left(\frac{\phi - \langle\phi\rangle_{FS}}{T_e}\right) - Z_i \nabla_{\perp} \cdot \left(\frac{n_0}{B_0 \omega_{c,i}} \nabla_{\perp}\phi\right) = Z_i \int dv J \cdot \left[\bar{F} - \bar{F}_{eq}\right], \tag{2}$$

$$B_{\parallel}^{\star}\dot{\mathbf{x}}_{GC} = v_{G\parallel}\mathbf{B}^{\star} + \frac{1}{Z_i}\mathbf{b} \times \nabla\Lambda, \tag{3}$$

$$B_{\parallel}^{\star} m_i \dot{v}_{G\parallel} = -\mathbf{B}^{\star} \cdot \nabla\Lambda. \tag{4}$$

Here, $\bar{F}$ is the gyrocentre distribution function, ϕ the electrostatic potential, $\mathbf{x}_{GC}$ and $v_{G\parallel}$ the gyro-center position and parallel velocity, Z_i and m_i the charge number and particle mass of Deuterium, B_0 the magnetic field amplitude, $\mathbf{b} = \mathbf{B}/\left\|\mathbf{B}\right\|$ and $B_{\parallel}^{\star} = \mathbf{B}^{\star} \cdot \mathbf{b} = B + \frac{m_i}{q_i} v_{G\parallel} \mathbf{b} \cdot (\nabla \times \mathbf{b})$ the phase space Jacobian defined through

$$\mathbf{B}^\star = \mathbf{B} + \frac{m_i}{q_i} v_{G\parallel} \nabla \times \mathbf{b}. \tag{5}$$

J is the gyro-average operator, $\mathcal{C}\left(\bar{F}\right)$ is the collision operator which conserves energy and particles [34], and $\Lambda = eZ_i J\left[\phi\right] + \mu B$ is the gyrocenter energy with $\mu = \frac{m_i v_\perp^2}{2B}$ the magnetic moment. $\mathcal{S}$ represents the source terms, including for example the heat source and/or the poloidal momentum (equivalent to a vorticity) source. $\langle \ldots \rangle_{FS} = \iint \ldots J_\chi d\theta d\varphi / \iint J_\chi d\theta d\varphi$ is the average over a flux-surface with $J_\chi = \left(\mathbf{B} \cdot \nabla\theta\right)^{-1}$ the flux-surface jacobian. The kinetic poloidal momentum source term, also referred as a vorticity source term, is defined as

$$\mathcal{S}_\Omega = \frac{m v_{G\parallel}^2 - \mu B}{T_s} S_r\left(r\right) S_0^\Omega \exp\left(-\frac{\frac{1}{2} m v_{G\parallel}^2 + \mu B}{T_s}\right) \tag{6}$$

with S_0 the source amplitude, $S_r\left(r\right)$ the radial profile and T_s the source temperature. The former two are GYSELA input parameters while the latter is fixed at $T_s/T_0 = 1$ and is a reference temperature. This source is built so that no heat nor particles are injected in the system. A marginal quantity of parallel momentum is injected along with the poloidal momentum as well as a pressure anisotropy. With the chosen parameters, the anisotropy is such that $P_\parallel/P_\perp \approx 2.4$ once the source saturates. As attested by [30], this anisotropy tends to destabilize the plasma and any transport barrier that could be generated through the vorticity source. The mathematical constructions of the heat and vorticity sources are detailed in [35] and [36]. The vorticity conservation equation is given by

$$\partial_t W + \partial_r \mathcal{K} = S_0 \nabla_\perp^2 S_r \tag{7}$$

with $W = -\left\langle \nabla \cdot \left(\frac{n_{eq,s} m_s}{B^2} \nabla_\perp \phi\right)\right\rangle_{FS} = e\left\langle \int dv^\star J \cdot \bar{F}\right\rangle_{FS}$ being the fluid vorticity , $\mathcal{K} = e\left\langle \int dv^\star J \cdot \left\{\left(d_t \mathbf{x}_G \cdot \nabla r\right) \bar{F}\right\}\right\rangle_{FS}$ the fluid vorticity flux and $S_0 \nabla_\perp^2 S_r$ the fluid vorticity source. Figure 1 (orange dashed line) represents the normalized fluid vorticity source profile as a function of the normalized radius. One can note the main central lobe at $r/a = 0.75$ which is later reffered as the source location. This equation is obtained by taking the gyro average of the Vlasov equation (1) and integrating over velocity space. A flux-surface average is then performed to obtain a 1D (i.e radial) equation for vorticity.

It can be difficult to inject a sheared radial electric field E_r in a full-f code; trying to inject such field directly in the quasi-neutrality equation proved to be uneffective [37] due to immediate screening effect of the plasma. Three different approaches are then possible to generate a $E \times B$ flow shear:

1. Impose a reversed radial safety factor profile $q(r)$ as studied in [37]. This method yielded no transport barrier behaviour and is not pursued here.

2. Use the poloidal momentum (also referred to as vorticity hereafter) source previously described. The idea is to add a term in the right-hand-side of the Vlasov equation (1) instead of the quasi-neutrality (2) to polarize the plasma. It adds a small term equivalent to a polarization density, effectively biasing locally the plasma and creating a local E_r field.

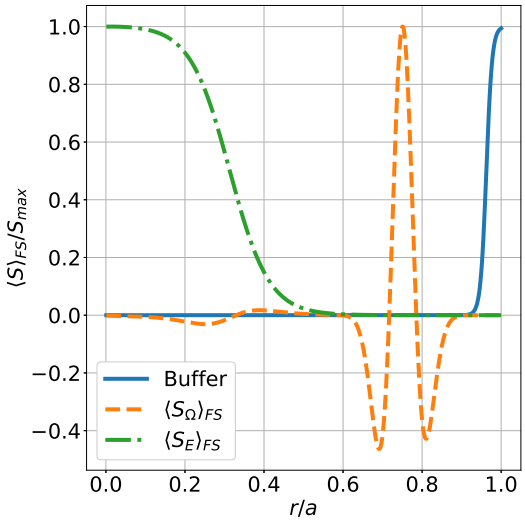

Figure 1: Normalized radial profiles of the buffer diffusion (blue line), fluid energy source (dotted green line) and fluid vorticity source (dashed orange line).

3. Locally change the radial force balance using a steep pressure gradient:

$$E_r = -\frac{1}{e_i n_i}\frac{\partial P_\perp}{\partial r} + v_\theta B_\varphi - v_\varphi B_\theta \tag{8}$$

Since radial transport is negligable with adiabatic electrons, we expect the imposed density gradient to remain and a sheared E_r to be generated to balance out the pressure gradient throughout the simulation. This case is referred as the steep gradient case hereafter. However, we expect the steep density gradient to stabilize linearly the ITG [7] and limit locally the turbulence level in the first place. This will be discussed in depth in section 5.

3 Parameters and saturation level

3.1 Simulation parameters

Three simulations with similar parameters are studied; the vorticity and reference cases are two branches of the same initial simulation where in the former the source is activated from $t\omega_{c,0} = 126400$ while the source stays deactivated in the latter. The third one is the so-called steep-gradient case. All of them use a normalized gyro radius $\rho^\star = \rho_0/a \equiv 1/200$ with ρ_0 the hydrogen Larmor radius and a the minor radius. The domain goes from $r/a = 0$ to $r/a = 1$ with the last 10% of the radial domain subject to a buffer diffusion region to damp out fluctuations at the edge and avoid possible numerical oscillations. Its radial profile is shown on figure 1 (solid blue line). Thus, the domain of interest is $r/a \in [0, 0.9]$. The isotropic heat source used in those simulations, localized in the interval $r/a = 0$ to $r/a \approx 0.4$ (See figure 1, green line), evolves in time; for the vorticity and reference cases, the amplitude of the source is fixed at a "high" value until turbulence intensity saturates. The heat source amplitude is then lowered so that the pressure profile stays roughly constant (i.e, its evolution becomes very slow in time). For the steep gradient case, the source amplitude is fixed at the same "high" value throughout the whole

duration of the simulation. Parameters are summarized in table 1.

3.2 Initial conditions

The initial temperature and density profiles are chosen such that ITG instabilities rise, meaning the ratio $\eta \equiv \frac{T^{-1}\partial_r T}{n^{-1}\partial_r n} = \kappa_T/\kappa_n = 3$ is constant on most of the domain except in the steep gradient case peaking at $\kappa_n \approx 15$ at $r/a = 0.75$ (see section 5) leading to $\eta \approx 0.44$. The vorticity case density profile (figure 2, dashed blue line) is close to a L-mode profile whereas the steep gradient one (figure 2, dotted orange line) is similar to what can be observed in H-mode discharges with a steep density gradient at the edge (See [21] for example).

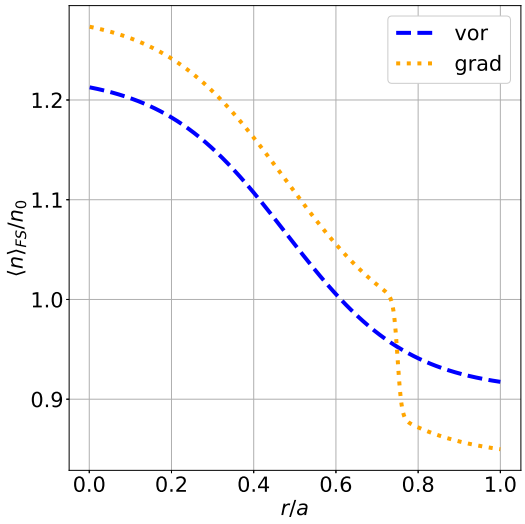

Figure 2: Radial profiles of the flux surface averaged guiding-center density at $t\omega_{c,0} = 0$ for the vorticity case (blue dotted line) and for the steep gradient case (orange dashed line).

3.3 Saturation level

We denote each mode as (n, m), where n and m are the toroidal and poloidal mode numbers. Figure 3 shows the time evolution of the $(0, 0)$ and $(0, 1)$ as well as some unstable (n, m) modes of the electrostatic potential at $r/a = 0.5$ in the reference simulation. All three simulations show very similar behaviours until the saturation happens since the parameters are almost identical, the steep density gradient at $r/a = 0.75$ being the only difference during the time frame shown hence the choice to only show the reference/vorticity case. The oscillating phase of the $(0, 0)$ and $(0, 1)$ modes from $t\omega_{c,0} = 0$ to $t\omega_{c,0} \approx 3 \cdot 10^4$ is due to the low frequency GAMs [38] (Geodesic Acoustic Modes). These oscillations are negligeable after the main plasma instability starts its linear growth, namely ITG. This linear growth phase starts at around $t\omega_{c,0} \approx 3 \cdot 10^4$ until turbulence saturation is reached at approximately $t\omega_{c,0} \approx 6 \cdot 10^4$ thanks to the rise of zonal flows. For each simulation, the global mean linear growth rate $2\overline{\gamma}_{lin} \approx 6 \cdot 10^{-4}\omega_{c,0}$ is computed by fitting the linear part on $E_k = \sum_{m,n} \phi^2_{m,n} - \phi^2_{0,0} - \phi^2_{0,\pm 1}$ (black line on figure 3), the perturbed potential energy at $r/a = 0.5$. Values for the different simulations are reported on table 1.

Parameters	Reference	Vorticity	Steep gradient
Charge / atomic numbers	$Z_i = 1, A_i = 2$		
Time step	$\Delta t\omega_{c,0} = 16$		
$N_r \times N_\theta \times N_\varphi \times N_{v_\parallel} \times N_\mu$	$511 \times 512 \times 64 \times 127 \times 31$		
Normalized gyroradius	$\rho^\star = \rho_{c,0}/a = 1/200$		
Inverse aspect ratio	$\epsilon = R_0/a = 4.4$		
Density	$\kappa_n = R/L_n = 2.2$	$\kappa_n = R/L_n = 2.2^*$	
Temperature	$\kappa_T = R/L_T = 6.6$		
Poloidal momentum amplitude	$S_0^\Omega = 0^{**}$	$S_0^\Omega = 0.08^{**}$	$S_0^\Omega = 0$
Average ITG linear growth rate	$\overline{\gamma_{lin}}/\omega_{c,0} \approx 3 \cdot 10^{-4}$		

Table 1: Simulation parameters used in this study. *For the steep gradient case, $\kappa_n \approx 15$ at $r/a = 0.75$ from $t\omega_{c,0} = 0$ until the end. **The poloidal momentum source is activated from $t\omega_{c,0} = 126400$ for the vorticity case and disabled in the reference case.

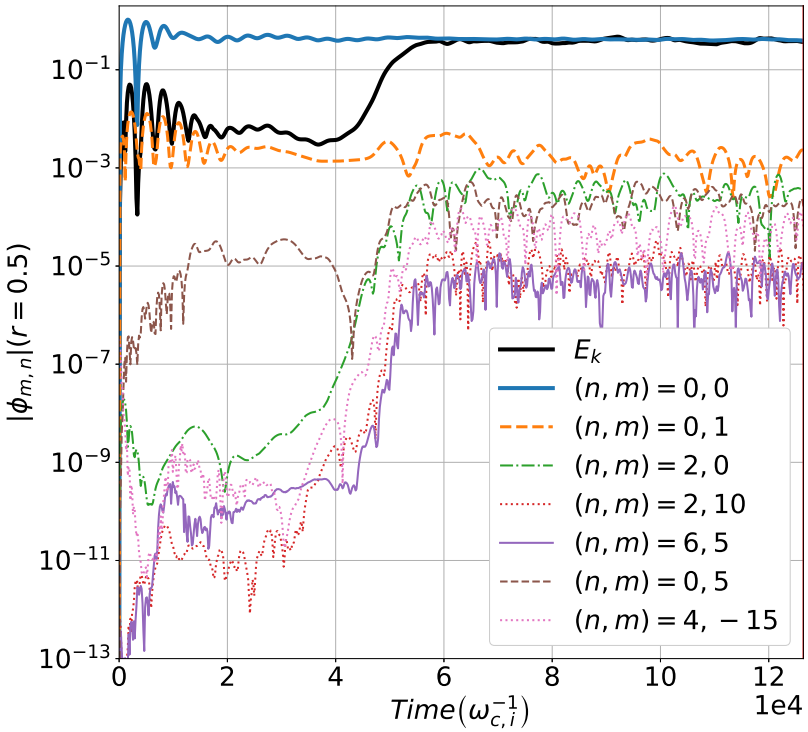

Figure 3: $\phi_{n,m}$ modes (i.e poloidal and toroidal, respectively) at $r = 0.5$ plotted against time (up to $t_{vor}\omega_{c,0} = 126400$, the vorticity activation time). The solid black line E_k represents the energy of the electrostatic potential perturbation and is used to compute the average linear growth rate of ITG modes. This plot is also representative of the steep gradient case since we look at the mode evolution at $r/a = 0.5$, away from the steep gradient region at $r/a = 0.75$.

4 Poloidal momentum (vorticity) source

4.1 Onset of a transport barrier

The source described in equation (6) is used to produce a sheared poloidal momentum profile to the system once turbulence intensity saturates and the pressure profile no longer shows any significant evolution. Figure 4a shows the $E \times B$ poloidal flow at the last simulation time for both the reference (green dotted line) and vorticity cases (blue dashed line). The vorticity source effectively injects the desired $E \times B$ flow shear compared to the reference case with a significant amplitude difference at $r/a = 0.7$ and $r/a = 0.8$. As stated in [39] and [30], it is empirically found in numerical simulations that the $\omega_{E\times B}$ shearing rate should be within the same order of magnitude as γ_{lin}^{MAX}, the maximum linear growth rate of the relevant instability (i.e ITG in this case) to stabilize the said instability. This simple rule of thumb is useful to have an idea of the amount of shear we should impose on the plasma *a priori*. Here we choose to normalize the shearing rate to $\overline{\gamma}_{lin} < \gamma_{lin}^{MAX}$ the average linear growth rate of the electrostatic potential Fourrier modes which is more representative of the actual "growth rate of ITG" instability. The idea is then to establish a shear flow around one order of magnitude higher than $\overline{\gamma}_{lin}$ (i.e $\omega_{E\times B} \approx 10\overline{\gamma}_{lin}$) to fullfil the previously discussed stabilizing conditions.

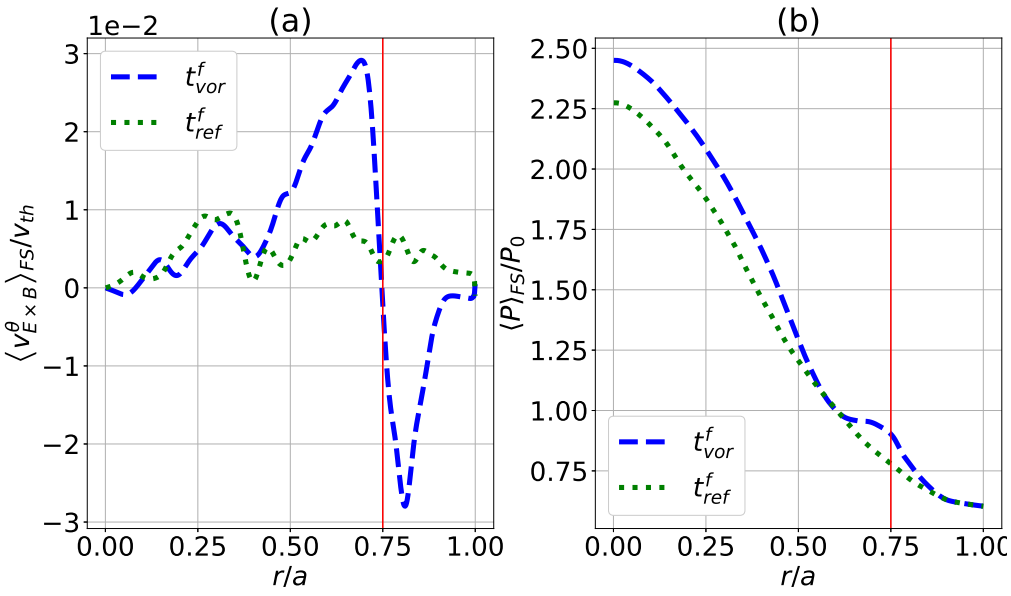

Figure 4: $E \times B$ velocity **(a)** and pressure **(b)** radial profiles at the end of the vorticity case t^f_{vor} and of the reference case t^f_{ref}. The red vertical line represents the vorticity source position if activated.

Figure 4b shows the radial pressure profiles of the reference (dotted green line) and vorticity (dashed blue line) at the last simulation time. Two main features appear when the source is turned on: a "plateau" appears at the source location and the core pressure increases relative to the reference case. This behaviour is necessarely due to the vorticity source since it is not observed in the reference case. The vorticity source used here does not inject energy in the system, and the heat source is the same as the reference case which means the increase seen on the radial profile is linked to the presence of some sort of transport barrier mechanisms.

To quantify the effect of such shearing conditions on confinement and turbulent heat transport of the main species, we choose to diagnose first the evolution of the effective heat diffusivity coefficient χ_T as a function of time in different radial regions by assuming heat transport is mainly diffusive, meaning $Q = -n\chi_T \nabla T$. For this purpose, we compute the radial perpendicular heat fluxes with

$$Q_\perp^{neo} = \overbrace{\int \mu B \left(\mathbf{v}_D \cdot \nabla r\right) \bar{F}_s dv}^{Q_{D,\perp}} + \overbrace{\int \mu B \left\langle \bar{\mathbf{v}}_{E\times B} \cdot \nabla r \right\rangle_\varphi \bar{F}_s dv}^{Q^{n=0}_{E\times B,\perp}}, \tag{9}$$

$$Q_\perp^{turb} = \underbrace{\int \mu B \left(\bar{\mathbf{v}}_{E\times B} \cdot \nabla r\right) \bar{F}_s dv}_{Q_{E\times B,\perp}} - Q^{n=0}_{E\times B,\perp} = Q^{n\neq 0}_{E\times B,\perp}. \tag{10}$$

The former is the neoclassical guiding-center heat flux, which is the sum of the neoclassical drift velocity contribution and the toroidally axisymmetric $E \times B$ drift contribution (i.e zonal flows and GAMs) while the latter is the turbulent guiding-center heat flux which consists in the non toroidally axisymmetric $E \times B$ drift contribution. Radial parallel heat fluxes are computed the same way by replacing μB by $\frac{1}{2} v_{G\parallel}^2$:

$$Q_\parallel^{neo} = \overbrace{\int \frac{1}{2} v_{G\parallel}^2 \left(\mathbf{v}_D \cdot \nabla r\right) \bar{F}_s dv}^{Q_{D,\parallel}} + \overbrace{\int \frac{1}{2} v_{G\parallel}^2 \left\langle \bar{\mathbf{v}}_{E\times B} \cdot \nabla r \right\rangle_\varphi \bar{F}_s dv}^{Q^{n=0}_{E\times B,\parallel}}, \tag{11}$$

$$Q_\parallel^{turb} = \underbrace{\int \frac{1}{2} v_{G\parallel}^2 \left(\bar{\mathbf{v}}_{E\times B} \cdot \nabla r\right) \bar{F}_s dv}_{Q_{E\times B,\parallel}} - Q^{n=0}_{E\times B,\parallel} = Q^{n\neq 0}_{E\times B,\parallel}. \tag{12}$$

Finally, we consider the total radial heat flux as the sum of all the turbulent and neoclassical contributions detailed from equations 9 to 12:

$$Q_{tot} = \overbrace{Q_\parallel^{turb} + Q_\perp^{turb}}^{Q_{tot}^{turb}} + \overbrace{Q_\parallel^{neo} + Q_\perp^{neo}}^{Q_{tot}^{neo}} \tag{13}$$

A radial average is then performed on equation 13 to get

$$\langle Q_{tot} \rangle_{\Delta r} = \left\langle Q_{tot}^{turb} \right\rangle_{\Delta r} + \langle Q_{tot}^{neo} \rangle_{\Delta r} \tag{14}$$

Assuming diffusive heat fluxes, one can write the different heat diffusivity components as follows:

$$\chi_T^{neo} = -\frac{\langle Q_\perp^{neo} \rangle_{\Delta r}}{\langle n \nabla T \rangle_{\Delta r}}, \tag{15}$$

$$\chi_T^{turb} = -\frac{\left\langle Q_\perp^{turb} \right\rangle_{\Delta r}}{\langle n \nabla T \rangle_{\Delta r}}, \tag{16}$$

$$\chi_T^{tot} = \chi_T^{turb} + \chi_T^{neo}. \tag{17}$$

The heat diffusivity coefficients are normalized to $\chi_{GB} = \rho^\star \chi_B = \rho^\star \frac{T_e}{q_i B}$, the gyro-Bohm diffusivity [40]. Both the turbulent and neoclassical channels are studied without the convection contribution since electrons are adiabatic and time-averaged particle transport vanishes. For this analysis, we select two radial regions:

- $\Delta r = [0.7, 0.8]$, the region where the flow shear is injected.
- $\Delta r = [0.38, 0.48]$, the region where the turbulence amplitude is found maximum.

Since a core pressure increase and a plateau are observed, a local decrease in diffusivity is expected as less energy is lost to the edge. Figures 6a and 7a show the time evolution of the spatial-averaged diffusivity coefficients in the source and core region regions respectively. The turbulent coefficient χ_T^{turb} quickly drops to zero in the source region (figure 6b, dotted blue line) when the poloidal momentum source is activated compared to the reference simulation (figure 6b, dashed orange line) which confirms the origin of the core presure increase and plateau. The neoclassical diffusivity χ_T^{neo} then becomes the main contributor to χ_T in this region due to the poloidal momentum source. Because of the B gradient along the major radius, the polarization created by the source is not purely poloidally symmetric and drives a small poloidal asymmetry in potential, which impacts the density profile through the quasi-neutrality equation (2), and ultimately pressure profile. The amount of vorticity injected is measured to be 30% higher for $\theta = 0$ than $\theta = \pi$. This affects locally the neoclassical transport but doesn't change the magnitude of χ_T^{neo}. Interestingly, the plasma core turbulent diffusivity (figure 7a and 7b) seems affected by the activation of the source even if it is not as impactful as near the source itself. Bursts are more noticeable and frequent in the core with the source than without (figure 7b, dashed orange line), but an overall decaying trend seems to take place after the source activation.

One can check the shear rate threhold at which the turbulence is suppressed by checking the evolution of the turbulent diffusivity χ_T^{turb} relative to the shear rate $\omega_{E\times B}$. A threshold at which the turbulence is suppressed appears clearly on figure 5 at around $\omega_{E\times B} \approx 3\overline{\gamma}_{lin}$, which is coherent with the rule of thumb presented previsouly.

The observed reduction in χ_T^{turb} can be explained through quasi-linear arguments. Let us consider a simple expression for the turbulent heat flux with $Q^r_{turb} = \left\langle P u^r_{E\times B} \right\rangle$ with $P = (n + \delta n)(T + \delta T)$ and $\delta u^r_{E\times B} \approx \frac{1}{B_0 r}\partial_\theta \delta\phi$, the δ referring to fluctuating quantities and $\delta u^r_{E\times B}$ the perturbed $E \times B$ drift velocity. This leads to:

$$Q^r_{turb} \approx \frac{1}{B_0 r}\left[\underbrace{\langle n\rangle \langle \delta T \partial_\theta \delta\phi\rangle}_{diffusion} + \underbrace{\langle T\rangle \langle \delta n \partial_\theta \delta\phi\rangle}_{convection}\right]. \tag{18}$$

From a linear point of view, $\delta T = \beta \delta\phi$ where β is a complex constant that can be determined through linear analysis. Then, from a quasi-linear standpoint, the $\langle \delta n \partial_\theta \delta\phi\rangle$ contribution to the turbulent heat flux is related to the Reynolds stress tensor $\Pi_{r\theta}$ and more generally to the convection term $T\Gamma \equiv \langle T\rangle \left\langle \delta n \delta u^r_{E\times B}\right\rangle$. Since electrons are adiabatic, this convection term vanishes. Considering a single poloidal mode for $\delta\phi$ such that $\delta\phi \propto \tilde{\phi}\exp\left[i\left(m\theta + n\varphi - \omega t\right)\right]$, we get

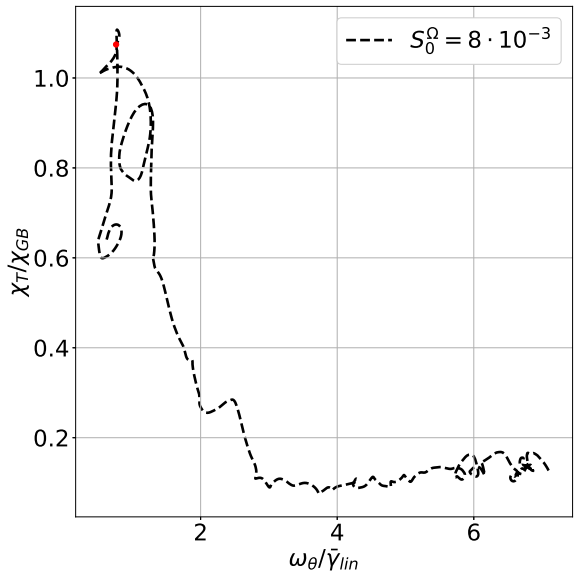

Figure 5: Turbulent heat diffusivity χ_T^{turb} plotted against the shear rate $\omega_{E\times B}$ in the source region $r/a = [0.7, 0.8]$ for $t\omega_{c,0} = [110400, 243200]$. The red dot represents the vorticity activation time for the vorticity case $t_{vor}\omega_{c,0} = 126400$.

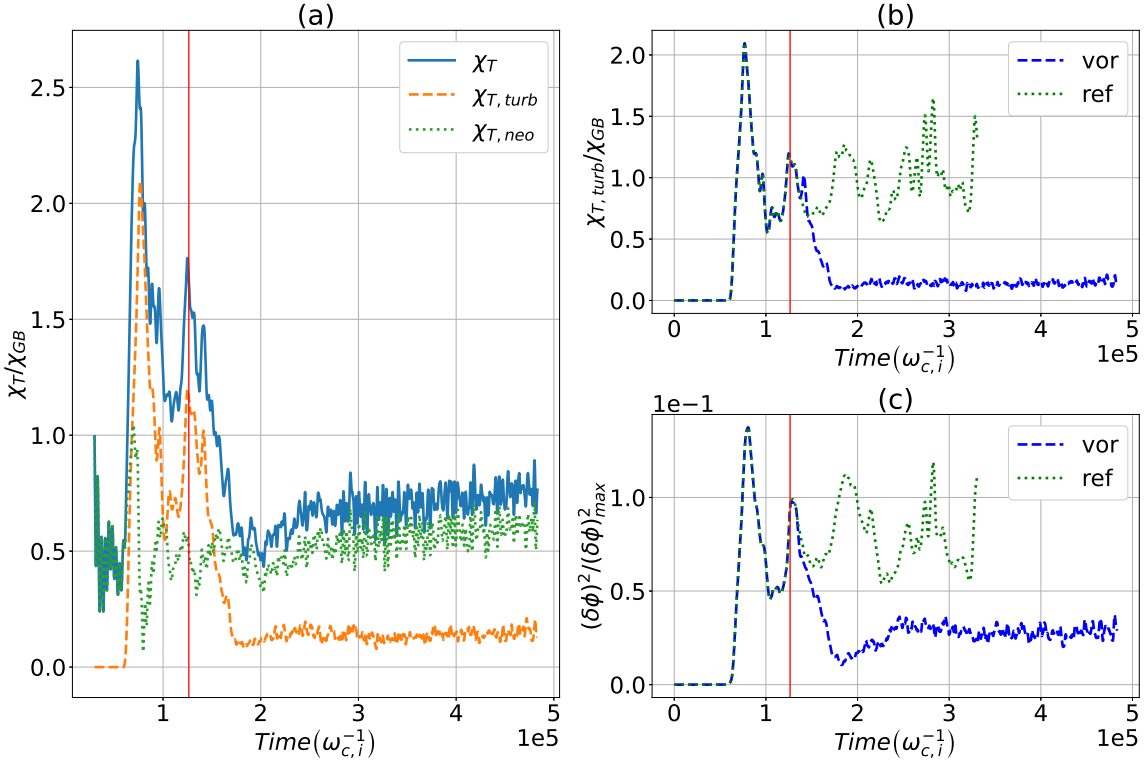

Figure 6: Diffusivity and turbulence intensity time evolution averaged in the $r/a = [0.7, 0.8]$ region. The red vertical line represents the vorticity activation time for the vorticity case. **(a)** Time evolution of the heat diffusivity coefficients for the vorticity case. **(b)** Turbulent contribution of the heat diffusivity as a function of time for the vorticity (blue dotted line, "vor") and reference cases (orange dashed line, "ref"). **(c)** Turbulence intensity plotted against time for the vorticity (blue dotted line, "vor") and reference cases (orange dashed line, "ref"). **(b)** and **(c)** signals are in phase.

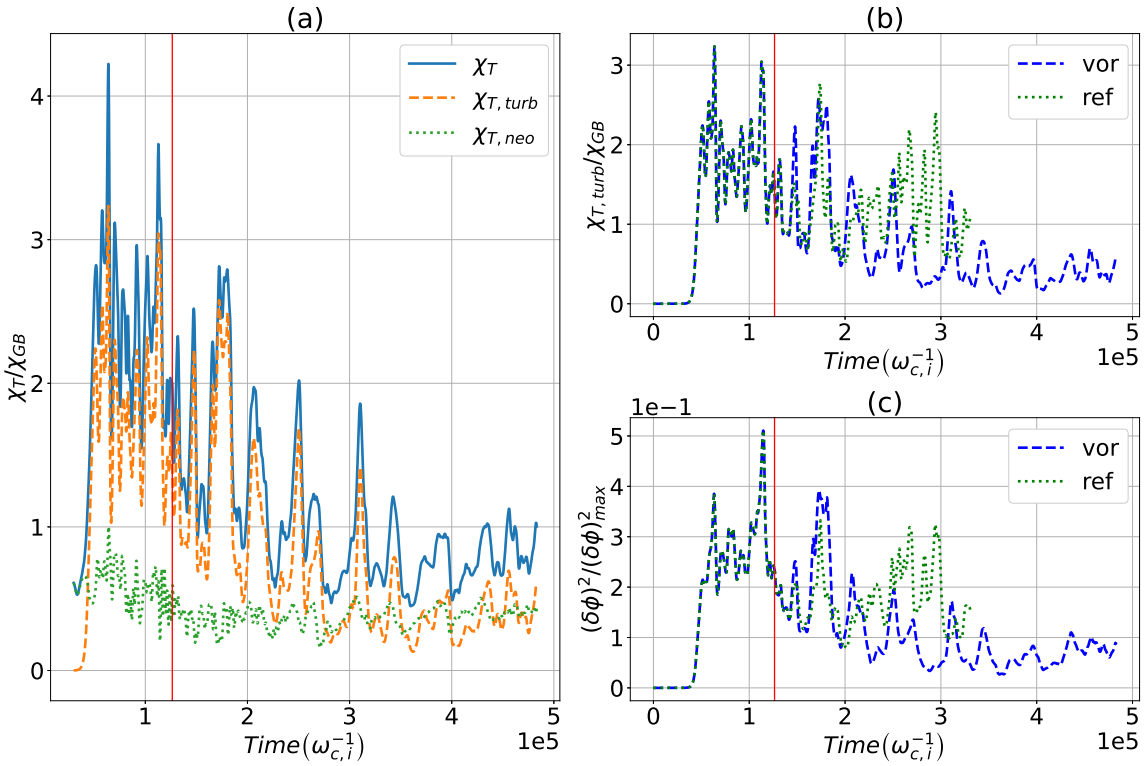

Figure 7: This figure is similar to figure 6 except that the radial average is in the $r/a = [0.38, 0.48]$ region. The red vertical line represents the vorticity activation time for the vorticity case. **(a)** Time evolution of the heat diffusivity coefficients for the vorticity case. **(b)** Turbulent contribution of the heat diffusivity as a function of time for the vorticity (blue dotted line, "vor") and reference cases (orange dashed line, "ref"). **(c)** Turbulence intensity plotted against time for the vorticity (blue dotted line, "vor") and reference cases (orange dashed line, "ref"). **(b)** and **(c)** signals are in phase.

$$Q^r_{turb} \approx \frac{\langle n \rangle}{B_0} \left\langle k_\theta \left(\delta\phi\right)^2 \right\rangle . \tag{19}$$

Equation (19) ultimately shows that $Q^r_{turb} \propto \left(\delta\phi\right)^2$ and reciprocally $\chi_T^{turb} \propto \left(\delta\phi\right)^2$. If the analysis presented here holds, $\left(\delta\phi\right)^2$ and χ_T^{turb} must be in phase. To verify this hypothesis, the following definition of electrostatic potential fluctuations is used:

$$\delta\phi\left(r,\theta,\varphi=0,t\right) = \phi\left(r,\theta,\varphi=0,t\right) - \left\langle \phi\left(r,\theta,\varphi\right)\right\rangle_\varphi , \tag{20}$$

$$\left\langle \delta\phi\right\rangle_{\theta,\Delta r} = \left\langle \delta\phi\left(r,\theta,\varphi=0,t\right)\right\rangle_{\theta,\Delta r} . \tag{21}$$

$\left\langle \phi\left(r,\theta,\varphi\right)\right\rangle_\varphi$ represents the toroidally axisymmetric modes of the potential and are substracted specifically to remove the contribution coming from :

- The mean potential, or the so-called $\phi_{0,0}$ Fourier mode, which is related to zonal flows [41].
- The convection cells [41], which are toroidally axisymmetric but exhibit poloidal asymetries noticeably produced by the vorticity source as discussed previously. They are associated with the $\phi_{m\neq 0,0}$ Fourier components.

The focus here is on a single poloidal plane $(r,\theta,\varphi=0)$ representative of the whole simulation box. The information of interest being the local turbulence intensity and later the radial and poloidal geometric structures, this will provide sufficient informations on those variables as discussed in [42] and [43].

Figures 6c and 7c represent the time evolution of the turbulence intensity in the source and core region respectively. As expected, those signals are in phase with χ_T^{turb} (figures 6b and 7b) in both regions, implying the previous relationship found between χ_T^{turb} and $\left(\delta\phi\right)^2$ holds in the case of adiabatic electrons. The turbulence intensity then largely decreases in the source region by a factor of 3. Note that there is still some lower level turbulence present locally. Moreover, the turbulence intensity also decreases in the core due to the source activation. The reduction in turbulent diffusivity is then directly linked to the reduction of turbulence intensity as deduced from the previous quasi-linear arguments.

4.2 Involved mechanisms: auto-correlation length and perpendicular wavenumber

As already discussed in the introduction, one of the main hypothesis is that an $E\times B$ flow shear is able to *tear* the turbulent structures locally to reduce their mean size and therefore stabilize the plasma. We propose two different approaches to verify this claim in our simulations:

1. Compute and compare the local auto-correlation radial length of the perturbed electrostatic potential for both the reference and vorticity cases. The aim is to check any shift or change in typical radial structure size.
2. Compute the poloidal wavenumber spectra of the perturbed electrostatic potential to monitor what scales are specifically affected by this turbulence intensity quench.

4.2.1 Auto-correlation radial length

The aim in this paragraph is to check whether we can see an effect on the "mean" size of turbulent structures due to the $E \times B$ shear flow. For this purpose, we calculate the fluctuations as written in equation (20) and then compute a correlation length Probability Density Function (PDF), following reference [42]:

$$C_{\delta\phi,\delta\phi}\left(r,\theta,\varphi=0,t,\delta r\right)=\frac{\sum_{\delta r}\delta\phi\left(r+\delta r,\theta,\varphi=0,t\right)\delta\phi\left(r,\theta,\varphi=0,t\right)}{\left[\delta\phi\left(r,\theta,\varphi=0,t\right)\right]^{2}} \tag{22}$$

This autocorrelation function is computed for each θ angle and radial location r on a radial window $[r-\delta r_{max}, r+\delta r_{max}]$. Here we adjust the radial extent to $\delta r_{max}=20\rho_{c,0}$, which is found to be sufficient to capture most of the turbulent radial structures. Thus we obtain a PDF for each time step, θ angle and radius $r/a \in [0.1, 0.9]$. The Half Width at Half Maximum (HWHM) of this PDF is taken along δr to obtain a time dependent poloidal map of the radial correlation length:

$$C_{\delta\phi,\delta\phi}\left(r,\theta,\varphi=0,t,L_{AC}^{\delta\phi}\right)=0.5. \tag{23}$$

Finally, the flux-surface average of the poloidal map obtained is computed before doing a time average over 3000 time steps ($3000\Delta t\omega_{c,0}=48000$).

$$\left\langle L_{AC}\right\rangle_{FS}\left(r\right)=\overline{\left\langle L_{AC}^{\delta\phi}\left(r,\theta,t\right)\right\rangle_{FS}}, \tag{24}$$

with the overline representing the time average.

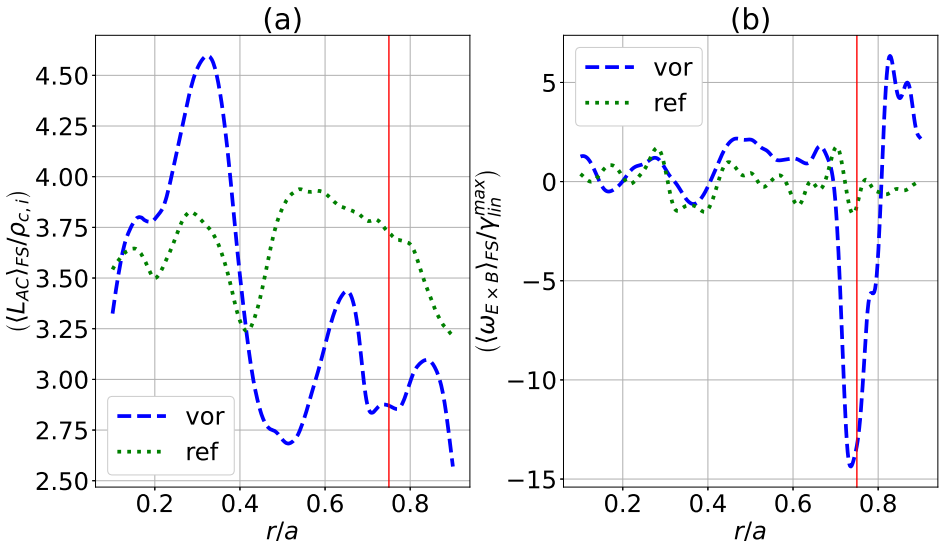

Figure 8: Flux surface and time average of the correlation length **(a)** and $E \times B$ shearing rate **(b)** as a function of radius for the reference (**"Ref"**) and vorticity (**"Vor"**) cases. The red vertical line indicates the source location.

Figure 8a shows the flux-surface and time averaged auto-correlation length as a fuction of the normalized radius while 8b shows the radial profile of the shear rate $\omega_{E\times B}$ at

the last simulation time. The reference case (figure 8a, dotted green line) represents the correlation length without the vorticity source. L_{AC} stays close to $3.5\rho_{c,i}$ with a small poloidal shearing level (figure 8b, dotted green line), but if the source is turned on (figure 8a, dashed blue line), the radial correlation decreases where the flow shear rate is maximal (figure 8b, dashed blue line), at $r/a = 0.75$, but also from $r/a = 0.45$ to $r/a \approx 0.9$. This is consistent with the turbulent structure shearing hypothesis: the $E \times B$ shear flow reduces locally the radial extension of the turbulent structures. This ultimately leads to a spatial decorrelation of those structures and a quench in turbulence intensity as previously observed. However, the correlation length increases in the range $r/a \in [0.2; 0.4]$, suggesting that the decrease of χ_T and thus turbulence intensity in that region is not the direct result of a local reduction in the auto-correlation length.

4.2.2 Poloidal wavenumber spectra

To complete this analysis, we compute the k_θ spectra of the perturbed electrostatic potential to monitor the intensity evolution of the different poloidal structure scales at different radius. The k_θ spectrum is computed through

$$\delta\phi\left(r,\theta,\varphi=0\right) \rightarrow I\left(r,k_\theta\right) = \overline{\left|\delta\phi\left(r,k_\theta,\varphi=0\right)\right|^2}. \tag{25}$$

For each time step, a 1D FFT is performed along the poloidal axis before averaging it over $1000\Delta t$ to get a cleaner signal. This is comparable to $I_{3D}\left(r,k_\theta\right) = \overline{\sum_{k_\varphi}\left|\delta\phi\left(r,k_\theta,k_\varphi\right)\right|^2}$ because the dominant modes are the resonant ones.
Figure 9a shows the core region (i.e $r/a = 0.43$) poloidal wavenumber spectra for the reference case (dotted green line) and vorticity case (dashed blue line). A lower turbulence intensity on most of the scales is observed except for $k_\theta\rho_{c,i} = 0.5$ and $k_\theta\rho_{c,i} = 0.1$ for the vorticity case compared to the reference case. However the spectra keeps most of its features without any striking changes; the poloidal extension of the core turbulence stays approximately the same with a slightly lower amplitude. Figure 9b shows the poloidal wavenumber spectra for the source region (i.e $r/a = 0.75$). A clear difference can be seen between the reference (dotted green line) and vorticity case (dashed blue line). The smallest poloidal scales ($k_\theta\rho_{c,i} > 0.1$) undergo a much more important decrease in intensity than the bigger ($k_\theta\rho_{c,i} < 0.3$) and especially the medium scales ($0.3 < k_\theta\rho_{c,i} < 0.6$). This shows a reorganisation of the turbulent structures at that location with a dominant scale shifting from $k_\theta\rho_{c,i} \approx 0.2$ to $k_\theta\rho_{c,i} \approx 0.1$, meaning the poloidal structures got bigger but also less intense. One explanation for this local shift is that turbulent structures may get *tilted* along the poloidal axis due to shearing as shown in figure 1 of [39]. As a result turbulent structures are radially smaller and poloidally bigger with an overall lower intensity.

5 Steep gradient case

Another way to generate a localized $E \times B$ poloidal shear flow is to produce a radially strong pressure gradient as shown with the radial pressure profile on figure 4a. Since the temperature profile is allowed to evolve (flux-driven condition) but not the ion density profile (adiabatic electrons), we can enforce an initial density profile with a steep gradient at the desired location, the pressure gradient intensity defining the poloidal shear flow

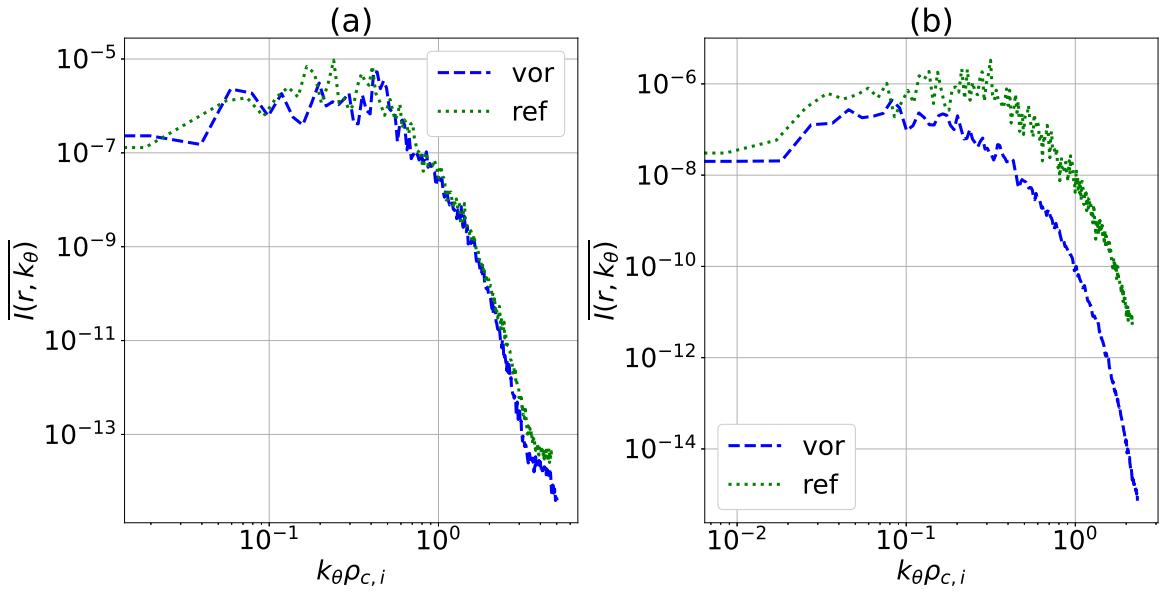

Figure 9: Poloidal wavenumber spectra using a 1D FFT averaged over the last 100 time steps for the reference (**Ref**) and vorticity (**Vor**) cases for $r/a = 0.43$ **(a)** and $r/a = 0.75$ **(b)**.

amplitude. A simulation with such gradient and characteristics detailed in table 1 shows that this method creates indeed the desired radial profile of poloidal $E \times B$ shear flow as shown in figure 10b. However, the velocity profile is different from the vorticity-induced one (figure 4b, dashed blue line) with a single lobe instead of 2 at $r/a = 0.75$. Otherwise, the $E \times B$ velocity profile is similar to what is observed to the reference case outside the steep gradient region.

Figure 11a shows the time evolution of the heat diffusivity components in the steep gradient region. The turbulent diffusivity is close to zero in that region and does not contribute heavily to the total diffusivity. Similarly, the turbulence intensity (figure 11c) does show the exact same trend as the turbulent diffusivity (figure 11b) and stays extremely low even compared to the turbulence intensity levels of the vorticity case. Moreover, the same decaying trend in the core as the vorticity case can be seen on figure 12a and 12b which correlates strongly again with the turbulence intensity in the same region as shown on figure 12c. This method then seems to be effective to reduce the heat turbulent transport coefficient and turbulence intensity both near the steep gradient and in the core. A similar transport barrier is then formed with this method.

The origin of the barrier is however more ambiguous than for the vorticity case. Two main factors need to be taken into account here.
The first one is the linear stabilization of ITG by the density gradient. One of the criteria to enable ITG to grow, roughly $\eta = \kappa_T/\kappa_n \geq 2$, is not satisfied in the steep gradient region from the start of the simulation with a local value of $\eta \approx 0.44$. The ITG modes are then linearly stabilized locally by the steep gradient in the first place.
Moreover, one cannot neglect the impact of the $E \times B$ shear flow generated by the pressure gradient. As shown on figure 8b and 13b, the shearing levels generated by the source and the steep gradient bear different shapes (i.e two vs one lobe) but are within the same order of magnitude of $\sim 10\bar{\gamma_{lin}}$. The $E \times B$ flow shear avoids ITG instabilities to grow by

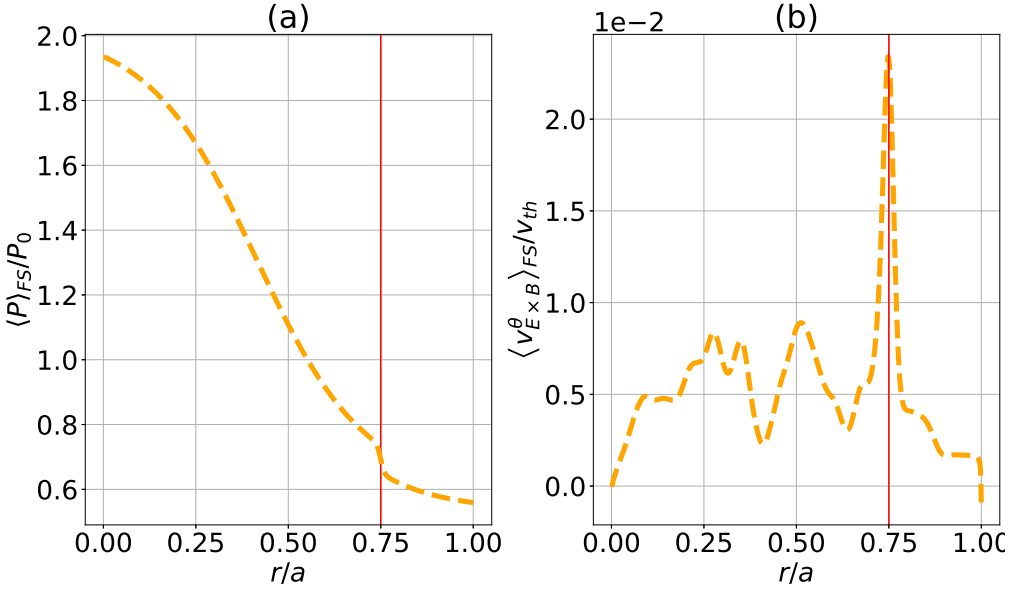

Figure 10: Radial profile of the total pressure **(a)** and $E \times B$ poloidal velocity **(b)** at the simulation end t^f for the steep gradient case. The red vertical line indicates the steep gradient position.

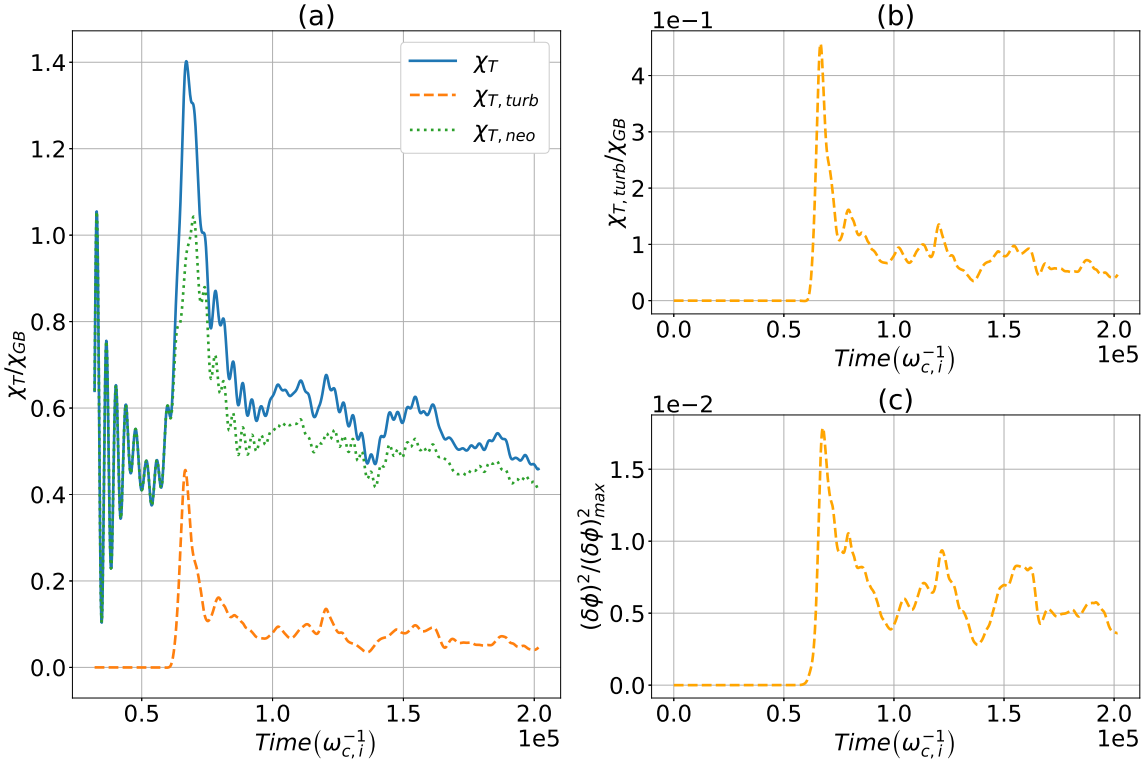

Figure 11: Diffusivity and turbulence intensity time evolution averaged in the $r/a = [0.7, 0.8]$ region. **(a)** Time evolution of the heat diffusivity coefficient for the steep gradient case. **(b)** Turbulent contribution of the heat diffusivity as a function of time for the steep gradient case. **(c)** Turbulence intensity plotted against time for the steep gradient case. **(b)** and **(c)** signals are in phase.

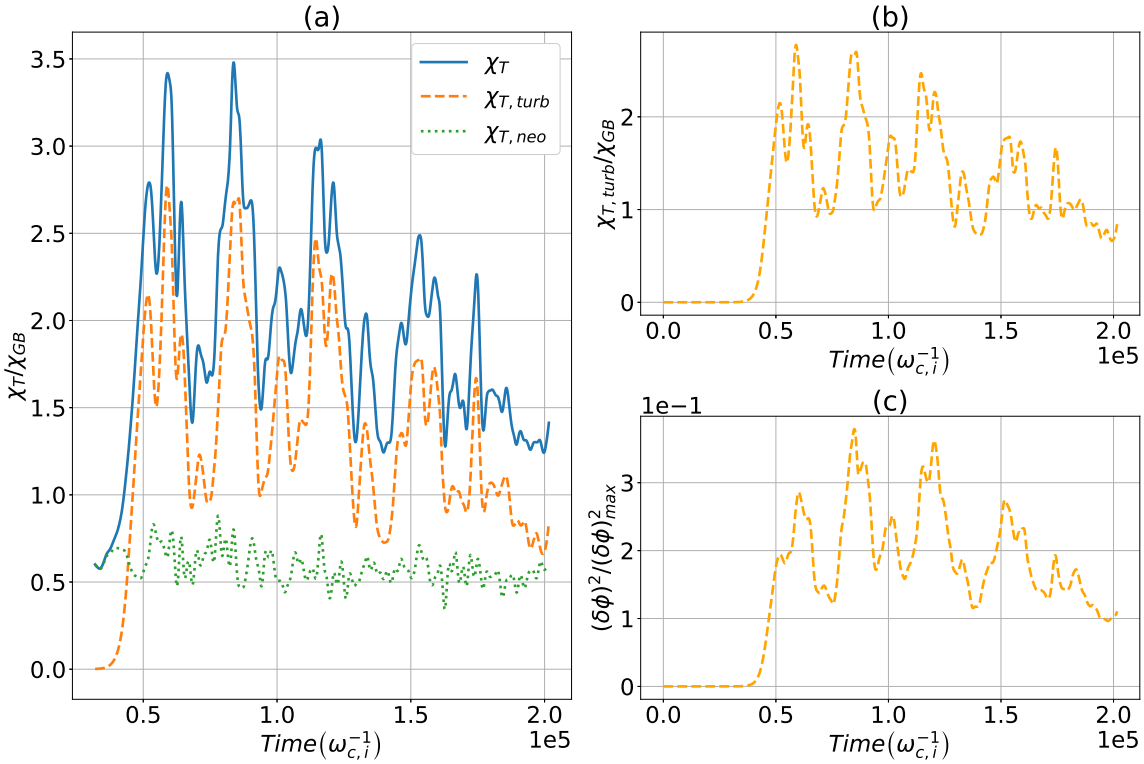

Figure 12: This figure is similar to figure 11 except that the radial average is in the $r/a = [0.38, 0.48]$ region. **(a)** Time evolution of the heat diffusivity coefficient for the steep gradient case. **(b)** Turbulent contribution of the heat diffusivity as a function of time for the steep gradient case. **(c)** Turbulence intensity plotted against time for the steep gradient case. **(b)** and **(c)** signals are in phase.

shearing radial turbulent structures that could develop either through non-linear interactions or turbulence diffusion. This results in an even more "effective" transport barrier with two different stabilizing mechanisms taking place simultaneously.

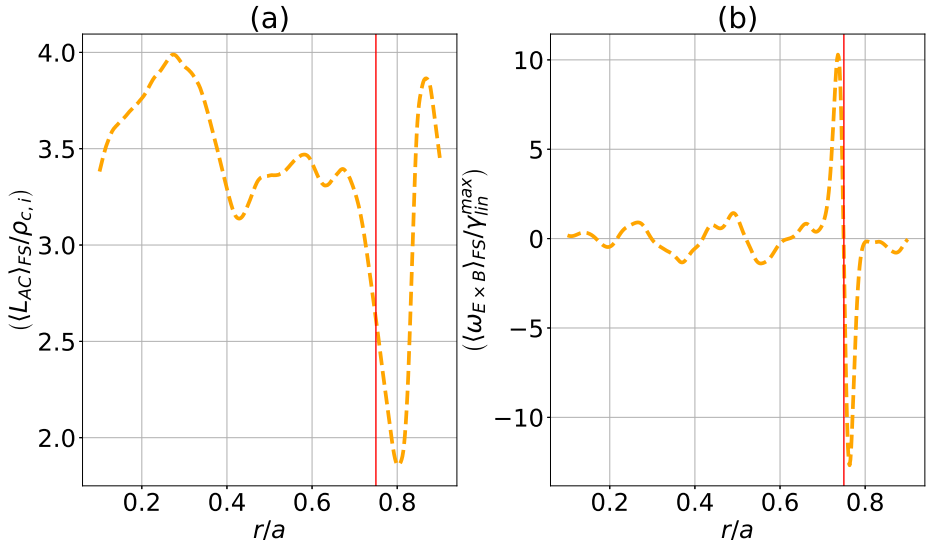

Figure 13: Flux surface and time average of the correlation length **(a)** and $E \times B$ shearing rate **(b)** as a function of radius for the steep gradient case. The red vertical line indicates the steep gradient location.

Figure 13a tends to confirm the previous analysis by showing that the auto-correlation radial length of the perturbed potential is significantly lower near the steep gradient position at $r/a = 0.75$. This shows that almost no turbulence structures are present here while the rest of the plasma shows a similar behaviour as the reference case shown of figure8b (dotted green line).

The k_θ spectrum completes this analysis: in the steep gradient region, the intensities of all poloidal scales are significantly lower than in the core region. This confirms the near-absence of turbulence in the steep gradient region and the barrier mechanism involved here.

6 Discussion and conclusion

We showed in this study using the GYSELA code two different ways to reduce turbulence and make the plasma transit to what can be described as an enhanced confinement mode with the development of a transport barrier.

The first way is based on a method proposed by A. Strugarek [30] [31] that uses a vorticity source to locally polarize the plasma to generate a strong $E \times B$ shear flow. This method leads to an immediate effect on the turbulent heat diffusivity χ_T^{turb} in the source region, going quickly to zero when the shear rate $\omega_{E\times B}$ reaches a threshold of $\omega_{E\times B} \approx 3\overline{\gamma}_{lin}$, meaning no fluctuations persist around the strongly sheared region. A reduction in χ_T^{turb} is observed as well in the core region compared to a reference case, showing that the edge-localized source has an impact on the core. One must note a side-effect on the local neoclassical transport by the source, the latter generating a poloidal

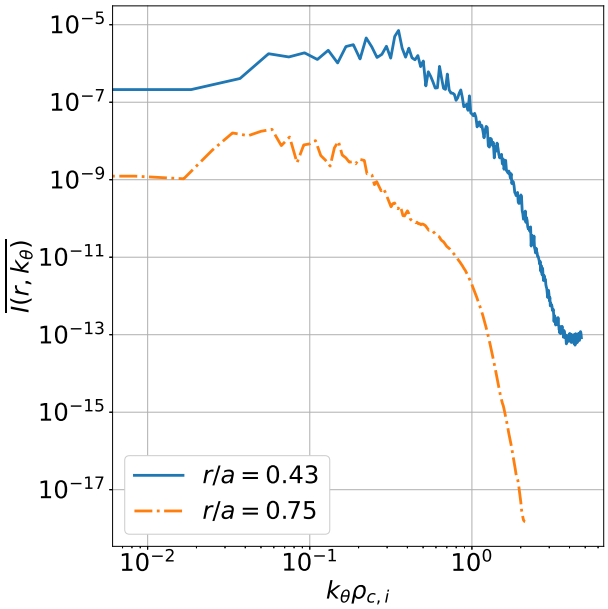

Figure 14: Poloidal wavenumber spectra for the steep gradient case for $r/a = 0.43$ (solid blue line) and $r/a = 0.75$ (dotted orange line).

asymmetry that leads to the former. This reduction in turbulence can be explained by the shearing of the larger turbulent structures into smaller ones as shown by the correlation length. The k_θ spectra analysis shows the impact of the source with lower turbulence intensity, shifting the maximum of the spectra to the lower wavenumber possibly due to the structures being tilted in the poloidal direction. This reduction in heat transport led to higher pressure in the core than the reference scenario without the vorticity source.

The second way consists in enforcing a H-mode-like density profile to generate through the force equilibrium a localized strong $E \times B$ shear flow. This alternate method managed to stabilize the plasma locally by linearly stabilizing ITG modes through the steep gradient profile enforced. In addition to this linear stabilization effect, the $E \times B$ flow shear generated by the steep pressure gradient also helps stabilizing the plasma by tearing apart any turbulent structures that could grow in the steep gradient region. The edge reduction in heat transport still leads to higher core temperatures, meaning the transport barrier created is efficient enough to increase energy confinement.

Acknowledgements

This work has been carried out within the framework of the EUROfusion Consortium, funded by the European Union via the Euratom Research and Training Programme (Grant Agreement No 101052200 — EUROfusion). Views and opinions expressed are however those of the author(s) only and do not necessarily reflect those of the European Union or the European Commission. Neither the European Union nor the European Commission can be held responsible for them. It was partly funded by the Agence Nationale de la Recherche for the project GRANUL (ANR-19-CE30-0005). This work was granted access to the HPC resources of IDRIS under special allocation spe00012 made by GENCI and of MARCONI under project FUA35 GSNTITE .

References

[1] F. Hinton and R. D. Hazeltine, "Theory of plasma transport in toroidal confinement systems," *Reviews of Modern Physics*, vol. 48, no. 2, p. 239, 1976.

[2] P. Donnel, *Impurity transport in tokamak plasmas: gyrokinetic study of neoclassical and turbulent transport*. PhD thesis, 2018.

[3] X. Garbet, P. Mantica, C. Angioni, E. Asp, Y. Baranov, C. Bourdelle, R. Budny, F. Crisanti, G. Cordey, L. Garzotti, *et al.*, "Physics of transport in tokamaks," *Plasma Physics and Controlled Fusion*, vol. 46, no. 12B, p. B557, 2004.

[4] T. Drouot, *Étude de la turbulence liée aux particules piégées dans les plasmas de fusion*. PhD thesis, Université de Lorraine, 2015.

[5] R. Waltz, G. Kerbel, and J. Milovich, "Toroidal gyro-landau fluid model turbulence simulations in a nonlinear ballooning mode representation with radial modes," *Physics of Plasmas*, vol. 1, no. 7, pp. 2229–2244, 1994.

[6] W. Tang, G. Rewoldt, and L. Chen, "Microinstabilities in weak density gradient tokamak systems," *The Physics of fluids*, vol. 29, no. 11, pp. 3715–3718, 1986.

[7] P. Guzdar, L. Chen, W. Tang, and P. Rutherford, "Ion-temperature-gradient instability in toroidal plasmas," *The Physics of Fluids*, vol. 26, no. 3, pp. 673–677, 1983.

[8] G. Lee and P. Diamond, "Theory of ion-temperature-gradient-driven turbulence in tokamaks," *The Physics of fluids*, vol. 29, no. 10, pp. 3291–3313, 1986.

[9] S. C. Prager, A. Sen, and T. Marshall, "Dissipative trapped-electron instability in cylindrical geometry," *Physical Review Letters*, vol. 33, no. 12, p. 692, 1974.

[10] T. Drouot, E. Gravier, T. Reveille, A. Ghizzo, P. Bertrand, X. Garbet, Y. Sarazin, and T. Cartier-Michaud, "A gyro-kinetic model for trapped electron and ion modes," *The European Physical Journal D*, vol. 68, no. 10, pp. 1–7, 2014.

[11] F. Wagner, G. Becker, K. Behringer, D. Campbell, A. Eberhagen, W. Engelhardt, G. Fussmann, O. Gehre, J. Gernhardt, G. v. Gierke, *et al.*, "Regime of improved confinement and high beta in neutral-beam-heated divertor discharges of the asdex tokamak," *Physical Review Letters*, vol. 49, no. 19, p. 1408, 1982.

[12] T. Kobayashi, "The physics of the mean and oscillating radial electric field in the l–h transition: the driving nature and turbulent transport suppression mechanism," *Nuclear Fusion*, vol. 60, no. 9, p. 095001, 2020.

[13] C. Bourdelle, "Staged approach towards physics-based lh transition models," *Nuclear Fusion*, vol. 60, no. 10, p. 102002, 2020.

[14] K. Burrell, S. Allen, G. Bramson, N. Brooks, R. Callis, T. Carlstrom, M. Chu, A. Colleraine, D. Content, J. DeBoo, *et al.*, "Confinement physics of h-mode discharges in diii-d," *Plasma Physics and Controlled Fusion*, vol. 31, no. 10, p. 1649, 1989.

[15] P. Gohil, K. Burrell, and T. Carlstrom, "Parametric dependence of the edge radial electric field in the diii-d tokamak," *Nuclear fusion*, vol. 38, no. 1, p. 93, 1998.

[16] K. Ida, "S, hidekuma, y, miura, t," *Fujita, M, Mori, K. Hoshino, N. Suzuki, T. YamauchiandJFT-2M Group: Phys. Rev. Lett*, vol. 65, p. 1364, 1990.

[17] R. McDermott, B. Lipschultz, J. Hughes, P. Catto, A. Hubbard, I. Hutchinson, R. Granetz, M. Greenwald, B. LaBombard, K. Marr, *et al.*, "the alcator c-mod group," *Phys. Plasmas*, vol. 16, p. 056103, 2009.

[18] Y. Andrew, N. Hawkes, T. Biewer, K. Crombe, D. Keeling, E. De La Luna, C. Giroud, A. Korotkov, A. Meigs, A. Murari, *et al.*, "Evolution of the radial electric field in a jet h-mode plasma," *EPL (Europhysics Letters)*, vol. 83, no. 1, p. 15003, 2008.

[19] E. Viezzer, T. Pütterich, G. Conway, R. Dux, T. Happel, J. Fuchs, R. McDermott, F. Ryter, B. Sieglin, W. Suttrop, *et al.*, "High-accuracy characterization of the edge radial electric field at asdex upgrade," *Nuclear Fusion*, vol. 53, no. 5, p. 053005, 2013.

[20] J. Schirmer, G. Conway, H. Zohm, and W. Suttrop, "the asdex upgrade team 2006," *Nucl. Fusion*, vol. 46, p. S780.

[21] R. Panek, J. Adámek, M. Aftanas, P. Bílková, P. Böhm, F. Brochard, P. Cahyna, J. Cavalier, R. Dejarnac, M. Dimitrova, *et al.*, "Status of the compass tokamak and characterization of the first h-mode," *Plasma Physics and Controlled Fusion*, vol. 58, no. 1, p. 014015, 2015.

[22] H. Meyer, C. Bunting, P. Carolan, N. Conway, M. Dunstan, A. Kirk, R. Scannell, D. Temple, M. Walsh, *et al.*, "The structure, evolution and role of the radial edge electric field in h-mode and l-mode on mast," in *Journal of Physics: Conference Series*, vol. 123, p. 012005, IOP Publishing, 2008.

[23] Z. Lin, T. S. Hahm, W. Lee, W. M. Tang, and R. B. White, "Turbulent transport reduction by zonal flows: Massively parallel simulations," *Science*, vol. 281, no. 5384, pp. 1835–1837, 1998.

[24] R. L. Dewar and R. F. Abdullatif, "Zonal flow generation by modulational instability," in *Frontiers in Turbulence and Coherent Structures*, pp. 415–430, World Scientific, 2007.

[25] P. H. Diamond, S. Itoh, K. Itoh, and T. Hahm, "Zonal flows in plasma—a review," *Plasma Physics and Controlled Fusion*, vol. 47, no. 5, p. R35, 2005.

[26] S. Kobayashi, Ö. D. Gürcan, and P. H. Diamond, "Direct identification of predator-prey dynamics in gyrokinetic simulations," *Physics of Plasmas*, vol. 22, no. 9, p. 090702, 2015.

[27] H. Biglari, P. Diamond, and P. Terry, "Influence of sheared poloidal rotation on edge turbulence," *Physics of Fluids B: Plasma Physics*, vol. 2, no. 1, pp. 1–4, 1990.

[28] K. Itoh and S.-I. Itoh, "The role of the electric field in confinement," *Plasma physics and controlled fusion*, vol. 38, no. 1, p. 1, 1996.

[29] P. Terry, "Suppression of turbulence and transport by sheared flow," *Reviews of Modern Physics*, vol. 72, no. 1, p. 109, 2000.

[30] A. Strugarek, Y. Sarazin, D. Zarzoso, J. Abiteboul, A. Brun, T. Cartier-Michaud, G. Dif-Pradalier, X. Garbet, P. Ghendrih, V. Grandgirard, *et al.*, "Ion transport barriers triggered by plasma polarization in gyrokinetic simulations," *Plasma Physics and Controlled Fusion*, vol. 55, no. 7, p. 074013, 2013.

[31] A. Strugarek, Y. Sarazin, D. Zarzoso, J. Abiteboul, A. Brun, T. Cartier-Michaud, G. Dif-Pradalier, X. Garbet, P. Ghendrih, V. Grandgirard, *et al.*, "Unraveling quasiperiodic relaxations of transport barriers with gyrokinetic simulations of tokamak plasmas," *Physical review letters*, vol. 111, no. 14, p. 145001, 2013.

[32] V. Grandgirard, J. Abiteboul, J. Bigot, T. Cartier-Michaud, N. Crouseilles, G. Dif-Pradalier, C. Ehrlacher, D. Esteve, X. Garbet, P. Ghendrih, *et al.*, "A 5d gyrokinetic full-f global semi-lagrangian code for flux-driven ion turbulence simulations," *Computer Physics Communications*, vol. 207, pp. 35–68, 2016.

[33] A. Brizard and T. Hahm, "Foundations of nonlinear gyrokinetic theory," *Reviews of modern physics*, vol. 79, no. 2, p. 421, 2007.

[34] P. Donnel, X. Garbet, Y. Sarazin, V. Grandgirard, Y. Asahi, N. Bouzat, E. Caschera, G. Dif-Pradalier, C. Ehrlacher, P. Ghendrih, *et al.*, "A multi-species collisional operator for full-f global gyrokinetics codes: Numerical aspects and verification with the gysela code," *Computer Physics Communications*, vol. 234, pp. 1–13, 2019.

[35] J. Abiteboul, X. Garbet, V. Grandgirard, S. Allfrey, P. Ghendrih, G. Latu, Y. Sarazin, and A. Strugarek, "Conservation equations and calculation of mean flows in gyrokinetics," *Physics of Plasmas*, vol. 18, no. 8, p. 082503, 2011.

[36] Y. Sarazin, V. Grandgirard, J. Abiteboul, S. Allfrey, X. Garbet, P. Ghendrih, G. Latu, A. Strugarek, G. Dif-Pradalier, P. Diamond, *et al.*, "Predictions on heat transport and plasma rotation from global gyrokinetic simulations," *Nuclear Fusion*, vol. 51, no. 10, p. 103023, 2011.

[37] Y. Sarazin, V. Grandgirard, P. Angelino, A. Casati, G. Dif-Pradalier, X. Garbet, P. Ghendrih, O. Gürcan, P. Hennequin, and R. Sabot, "Turbulence spectra and transport barriers in gyrokinetic simulations," in *AIP Conference Proceedings*, vol. 1069, pp. 325–330, American Institute of Physics, 2008.

[38] N. Winsor, J. L. Johnson, and J. M. Dawson, "Geodesic acoustic waves in hydromagnetic systems," *The Physics of Fluids*, vol. 11, no. 11, pp. 2448–2450, 1968.

[39] K. Burrell, "Effects of exb velocity shear and magnetic shear on turbulence and transport in magnetic confinement devices," tech. rep., General Atomic Co., 1996.

[40] R. Waltz, J. Candy, and M. Rosenbluth, "Gyrokinetic turbulence simulation of profile shear stabilization and broken gyrobohm scaling," *Physics of Plasmas*, vol. 9, no. 5, pp. 1938–1946, 2002.

[41] P. Donnel, X. Garbet, Y. Sarazin, Y. Asahi, F. Wilczynski, E. Caschera, G. Dif-Pradalier, P. Ghendrih, and C. Gillot, "Turbulent generation of poloidal asymmetries

of the electric potential in a tokamak," *Plasma Physics and Controlled Fusion*, vol. 61, no. 1, p. 014003, 2018.

[42] P. Ghendrih, G. Dif-Pradalier, C. Norscini, T. Cartier-Michaud, D. Estève, X. Garbet, V. Grandgirard, G. Latu, C. Passeron, and Y. Sarazin, "Self organisation of plasma turbulence: impact on radial correlation lengths," in *Journal of Physics: Conference Series*, vol. 561, p. 012008, IOP Publishing, 2014.

[43] P. Ghendrih, C. Norscini, T. Cartier-Michaud, G. Dif-Pradalier, J. Abiteboul, Y. Dong, X. Garbet, O. Gürcan, P. Hennequin, V. Grandgirard, *et al.*, "Phase space structures in gyrokinetic simulations of fusion plasma turbulence," *The European Physical Journal D*, vol. 68, no. 10, pp. 1–17, 2014.